Experimental Evaluation of the Concentrated Solar Heat Flux Distribution Provided by an 8 M2 Scheffler Reflector

Gabriel Guillet, Jonathan Gaspar, Séverine Barbosa, Thomas Fasquelle, Benjamin Kadoch

Highlights

Experimental evaluation of the concentrated solar heat flux distribution provided by an 8 m² Scheffler reflector

Gabriel Guillet, Jonathan Gaspar, Séverine Barbosa, Thomas Fasquelle, Benjamin Kadoch

- The concentrated heat flux distribution of an 8 m² Scheffler reflector is described
- The characterisation is based on thermography and inverse techniques
- The heat flux distribution observed can be approximated by a 2D Gaussian function
- The mean major and minor diameters of the distribution are 45 cm and 37 cm
- The area and heat flux concentration ratios are respectively 39 and 25

Experimental evaluation of the concentrated solar heat flux distribution provided by an 8 m² Scheffler reflector

Gabriel Guillet[a], Jonathan Gaspar[a], Séverine Barbosa[a], Thomas Fasquelle[a,*], Benjamin Kadoch[a]

[a] *Aix Marseille Univ, CNRS, IUSTI, Marseille, France*

Abstract

This study gives experimental results on the intensity and distribution of the concentrated heat flux delivered by an 8 m^2 Scheffler reflector located in Marseille, France (lon. 5.4° E, lat. 43.3° N). Using thermography and inverse techniques, detailed maps of heat flux densities on a vertical screen were obtained at different times and on different days. The heat flux distributions provided were successfully fitted to a two-dimensional Gaussian model. The model parameters were used to objectively calculate, among other things, the mean major and minor diameters of the ellipse containing 99.7 % of the heat flux, i.e. 45 cm and 37 cm respectively. Maximum heat flux densities ranged between 81 $kW \cdot m^{-2}$ and 112 $kW \cdot m^{-2}$ and the total heat fluxes delivered by the reflector were between 2.4 kW and 3.2 kW, which led to energy efficiencies between 61 % and 67 %. The issue of repeatability of measurements and seasonal/daily variations is also discussed. The results of this study could serve as a basis for the development of realistic numerical models and be useful to engineers responsible for optimising systems incorporating a Scheffler reflector.

Keywords: solar energy concentration, Scheffler reflector, heat flux distribution, thermography, inverse techniques

*Corresponding author.

Email address: thomas.fasquelle@univ-amu.fr, Postal address: 5 Rue Enrico Fermi, 13453 Marseille, France (Thomas Fasquelle)

Nomenclature

Latin symbols		**Units**
A	surface area of the reflector	m^2
A_{ef}	effective reflecting surface of the reflector	m^2
A_{ap}	aperture area of the reflector	m^2
A_{abs}	surface area of the solar absorber	m^2
A_i	surface area of the image	m^2
C_a	area concentration ratio	
$C_{f,\,av}$	average heat flux density concentration ratio	
f	focal length	m
h	convective heat exchange coefficient	$\mathrm{W \cdot K^{-1} \cdot m^{-2}}$
I	direct normal irradiance	$\mathrm{W \cdot m^{-2}}$
k	coverage factor	%
n	nth day of the year	
$\dot{Q}_{in}$	total heat flux collected by the reflector	W
$\dot{Q}_{out}$	total heat flux delivered by the reflector	W
T	temperature	°C
$W_{x1,\,99.7\%}$	width on x_1 axis of the ellipse containing 99.7 % of the heat flux	mm
$W_{y1,\,99.7\%}$	width on y_1 axis of the ellipse containing 99.7 % of the heat flux	mm
$(O, \mathbf{e}_x, \mathbf{e}_y, \mathbf{e}_z)$	reference frame	
$(C, \mathbf{e}_{x1}, \mathbf{e}_{y1}, \mathbf{e}_z)$	reference frame of the heat flux distribution	
(x, y, z)	coordinates according to the reference frame $(O, \mathbf{e}_x, \mathbf{e}_y, \mathbf{e}_z)$	W
(x_c, y_c)	coordinates of the centre C of the heat flux distribution	W

Greek symbols	**Units**

α	solar absorptivity	
β	angle between the reflector plane and the vertical	$^\circ$
ξ	sun elevation angle at noon	$^\circ$
δ	solar declination	$^\circ$
ε_c	mean spectral emissivity of cast-iron	
ε_p	mean spectral emissivity of the paint	
ζ	section plane angle	$^\circ$
η_{cov}	coverage factor of the reflector	
η_{ref}	energy efficiency of the reflector	
γ	intercept factor	
θ	rotation angle of the heat flux distribution	$^\circ$
κ	thermal conductivity	$\mathrm{W \cdot K^{-1} \cdot m^{-1}}$
λ	wavelength	m
ρ	global reflectivity	
ρ_{spec}	specular reflectivity	
σ_{x1}	standard deviation of the heat flux distribution on x_1 axis	mm
σ_{y1}	standard deviation of the heat flux distribution on x_1 axis	mm
σ_{max}	maximum standard deviation observed	mm
φ	heat flux density	$\mathrm{W \cdot m^{-2}}$
φ_{max}	maximum heat flux density	$\mathrm{W \cdot m^{-2}}$
φ_{offset}	offset heat flux density	$\mathrm{W \cdot m^{-2}}$
Ω	slab domain	
ψ	inclination of the rotation axis of the reflector	$^\circ$

1. Introduction

While the world's demand for energy is constantly increasing, the massive extraction and use of depleting fossil resources to meet this need is responsible for many burdens, including climate change. In this context, the solar resource appears to be one of the keys to the problem, along with sobriety. Indeed, though being erratic, it is distributed over the Earth's surface, available for free and will never be depleted on a human timescale.

Solar thermal energy is frequently used for both small scale and large scale applications, *i.e.* from domestic hot water production to electricity production with a solar tower. Medium scale applications such as cooking, drying and distillation are still scarce [1]. There is therefore a need for cost-effective and energy-efficient solar concentrating systems in order to compete with regular fossil fuel machines. Due to its ingenious design and easy handling, Scheffler reflector could be a solution for these applications [2].

A Scheffler reflector is a flexible parabolic-type reflector which serves to concentrate solar rays to a fixed point that can be indoor. As in Figure 1, a secondary reflector can optionally be used to reorient the rays in another direction and shift the focal point [3].

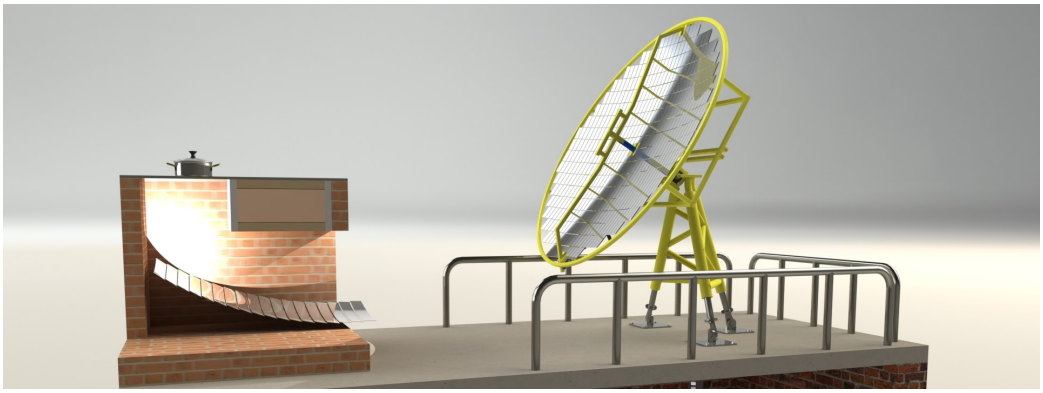

Figure 1: Representation of a solar cooker using a Scheffler reflector and a curved secondary reflector. The Scheffler reflector concentrates the sunlight, while the secondary reflector redirects the concentrated heat flux under the cooking plate.

Since Scheffler reflectors have been introduced in the scientific literature [3], their geometric characteristics have been studied [1], and more recently, charts have been realised to facilitate their fabrication [4].

Most of the studies are theoretical works and assume that the contour of the heat flux distribution has an elliptical shape. For example, Dib and

Fiorelli [5] studied the theoretical size of the area receiving heat flux at the focus of a standing reflector having an aperture area of $1\,m^2$ at equinox. They showed that this ellipse area is larger in summer than in winter due to optical imperfections, the tilt of the reflector and the declination of the sun. Reddy and Khan obtained more accurate information on the heat flux distribution thanks to ray-tracing simulations. They were thus able to study the effect of some adjusting parameters, *i.e.* the mirrors' size and the tracking delay [6]. Fontani *et al.* [7] also brought information on dispersion caused when bending the reflector, combining mechanical simulation and ray-tracing analysis.

Nevertheless, theoretical and numerical studies have produced highly variable results, as little is known about the actual characteristics of Scheffler reflectors (which are closely related to the hand-crafted manufacturing process). Indeed, there are only a few experimental studies providing detailed data. Oelher and Scheffler [3] reported that their $8\,m^2$ reflector, having an aperture of $4.7\,m^2$ at the date of the measurement, could deliver 2.1 kW at the focus on a 0.6 m diameter area. This leads to an energy efficiency of 60 % and a concentration ratio of 16.6. This was an important first data set, however it does not give details on the heat flux distribution on the absorber.

Other studies have given the overall energy efficiency of a Scheffler reflector combined with an absorber, often referred to as "optical efficiency". One can cite Ayub *et al.* [8] and Kanyowa *et al.* [9], who measured respectively optical efficiencies of 37 % to 65 %, and 70 % to 80 %. However, this does not give any information about the Scheffler reflector alone, nor about the heat flux distribution at the focus.

Ayub *et al.* [8] measured energy and exergy efficiencies on an experimental baking oven powered by a $10\,m^2$ Scheffler reflector. They studied the global system, the reflector and absorber together, and the oven, using calorimetric techniques while baking cakes at 180 °C (transient state). Kanyowa *et al.* [9] studied a bigger system constituted of 14 pairs of $10\,m^2$ Scheffler reflectors which provides steam to feed a kitchen serving 2000 to 6000 meals per day. Calorimetric measurements were carried out on one pair of reflectors and its absorber while assuming steady-state. The authors mentioned the reflectivity of the mirrors but the overall efficiency of the reflector cannot be deduced from this.

Chandrashekara *et al.* worked on the desalination performance of a $2.7\,m^2$ Scheffler reflector, using an exfoliated graphite receiver coating and two energy storage systems. They reported an overall efficiency up to 40 % between incoming solar power on the reflector's aperture plane and the desalination

power [10, 11].

Alberti [12] further investigated the intensity and distribution of heat flux in the focal zone. He observed that the light focused by a $2\,m^2$ reflector was contained in a 15 cm square and stated that most of the energy would certainly be contained in a 5 cm square. An image of the heat flux distribution at the focus is provided (using moonlight instead of sunlight), but not enough methodology is presented to conclude quantitatively on the performance of the reflector used. Finally, in their description of a marmalade factory, Pulfer *et al.* [13] mentioned that the diameter of the "focus area" generated by the $4.5\,m^2$ Scheffler collector is approximately 0.4 m which is again only an order of magnitude.

Sasidharan and Dutta [14] attempted to bring more details. They measured the heat flux in the focal area of a $32\,m^2$ reflector with 5 fluxmeters. Then, they built a 3D numerical model of the Scheffler reflector and refined the experimental data by ray-tracing. As a result, a random heat flux distribution was obtained on the focal plane and the total heat flux hitting the target was estimated to 860 W. According to them, the difference between the theory and their results can be explained by the integration of ray spillage and reflector surface characteristics in the simulation.

Accurate evaluations are rare, probably because evaluating the distribution of concentrated sunlight in the focal area is not a trivial task. It requires a detection system with a wide field of view, high spatial resolution and high heat flux resistance. The methods that are commonly used in the concentrated solar power field [15] require cooled Lambertian screens (*i.e.* with an assumed total diffusive reflection), a Charged-Coupled Device (CCD) camera and a cooled flux sensor. The procedure is as follows; For calibration, the flux sensor is positioned at a given point of the focal plane and measures a reference solar heat flux concentrated at this precise location; The Lambertian screen is then placed in the focal plane while the CCD camera records the brightness distribution at its surface; The heat flux is estimated from the reference flux and the comparison of the gray shades of the pixels.

Several variants of this technique have been proposed and compared, all showing relatively low uncertainty on estimates, and with different complexities [15], *e.g.* i) a system with moving parts can be used to avoid cooling, ii) a large amount of heat flux sensors can be applied to obtain a large heat flux map from their interpolation, iii) a coupling between optical modelling and measurements can be considered, iv) the actual absorber can be acted as the measurement surface with calorimetry, v) the flux distribution can

be estimated from the total heat flux, the mirror's reflectivity and the grey levels obtained with a non-calibrated CCD camera.

With this last method, Dib [16] assessed the heat flux distribution on a receiving screen in the focal area of a Scheffler collector, which is located in São Paulo, Brazil (lat. -23.65°) and which has an aperture area of $2\,\mathrm{m}^2$ ($2.7\,\mathrm{m}^2$ collector area). The authors used a CMOS (Complementary Metal-Oxide-Semiconductor) camera instead of CCD and found heat flux densities up to $377\,\mathrm{kW}\cdot\mathrm{m}^{-2}$ distributed in an ellipsoidal shape. Depending on the day of the year, the major axis (major diameter) of the latter was ranging from $0.252\,\mathrm{m}$ to $0.348\,\mathrm{m}$ and the minor axis (minor diameter) from $0.284\,\mathrm{m}$ to $0.293\,\mathrm{m}$.

The objective of this work is to provide the heat flux distribution characteristics of an $8\,\mathrm{m}^2$ Scheffler collector. The method is based on measurements on a screen with a high resolution infrared camera, coupled with a heat transfer model and inverse techniques. This method has already been developed in previous works, notably for nuclear energy research [17], and can also be applied to concentrating solar systems. It can be used to evaluate the heat flux distribution directly on an interface, with or without complex secondary optics that would make the use of conventional techniques more complicated. The novelty of this work is therefore twofold: the originality of the technique for concentrated solar power application and the supply of currently lacking detailed experimental data on $8\,\mathrm{m}^2$ Scheffler collectors.

For this purpose, Section 2 gives the description of the experimental test-bench and procedure. Then, Section 3 details the results and compares the heat flux distribution with the curve of a two-dimensional Gaussian function. Finally, conclusions and perspectives are given in Section 4.

2. Materials and methods

2.1. Main principles

Understanding the behaviour and assessing the performance of a reflector requires to know the characteristics of the heat flux it collects $\dot{Q}_{in}$ (input) and delivers $\dot{Q}_{out}$ (output). The test bench is shown in Figure 2. The heat flux collected is assessed using the aperture of the reflector and the solar direct normal irradiance recorded by a pyrheliometer. The heat flux delivered by the reflector is collected by a cast-iron screen (receiver) positioned vertically in the reflector focal plane. This radiation is absorbed and diffused into the screen by conduction. Part of the heat is stored in the material

and increases its temperature, while the other part is released into the environment by convection and radiation. Measurements of air temperature and wind velocity are used to evaluate convective and radiative exchanges with the environment. An infrared camera measures the radiation emitted by the back of the screen, and the emissivity of the emitting surface is used to deduce the temperature field. From this temperature field, a thermal model of the screen and inverse techniques are used to estimate the heat flux initially absorbed by the screen. The solar absorptivity of the screen is then used to obtain the heat flux delivered by the reflector. A regression analysis against a two-dimensional Gaussian model is performed to deduce quantitative information about the distribution (especially its size). The main steps of the method are summarised in Figure 3.

2.2. Scheffler reflector

The Scheffler reflector studied has a focal length f of about 1.47 m and a theoretical surface area A of $8\,\mathrm{m}^2$ (same characteristics as the one described by Munir [1]).

The surface area is composed of hundreds of flat mirrors of 8 cm x 10 cm and 2.5 cm x 15 cm, made of a thin reflective sheet covered by a layer of glass. As the reflector under study was built in 1999, it has been renovated several times. Consequently, some mirrors have been replaced and the mirrors covering the reflector are not all of the same reflectivity. Thus, reflectivity measurements were carried out and the overall global solar reflectivity ρ of the reflector was estimated at $80\,\% \pm 5\,\%$ using an area-weighted average of the reflectivity of the mirrors.

The mirrors do not cover the complete surface of the reflector due to spacing between themselves, the elliptical shape of the reflector and the small photovoltaic module used to power the sun tracking system (see Figure 2a). Thus, the effective reflective area A_{ef} is estimated to $7.5\,\mathrm{m}^2 \pm 0.3\,\mathrm{m}^2$. This area loss can be expressed as a coverage factor η_{cov} of $94\,\%$ which specifies the proportion of the collector theoretical area that is effectively covered with a reflective material.

The reflector is also equipped with an electronic sun tracking device. It consists of two photodiodes separated by a wall and connected to an electronic board (Arduino Uno) that controls a small motor. The device ensures the sun tracking by rotating the reflector until both photodiodes receive a similar amount of sunlight.

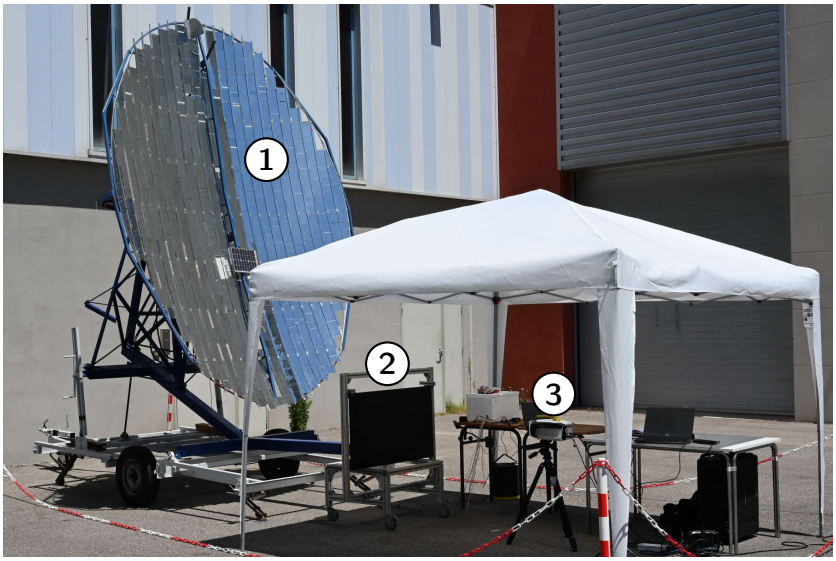

(a)

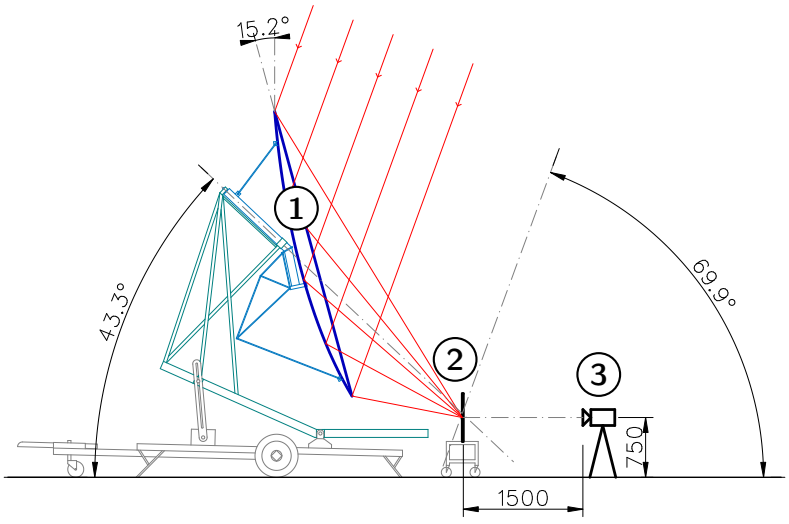

(b)

Figure 2: Picture (a) and schematic diagram (b) of the test bench on 14/06/2022. The Scheffler reflector (1) focuses the sun light directly on the cast-iron slab (2). This last one is vertical and painted in black at the face observed by the infrared camera (3). Distances are given in millimetres and angles in degrees.

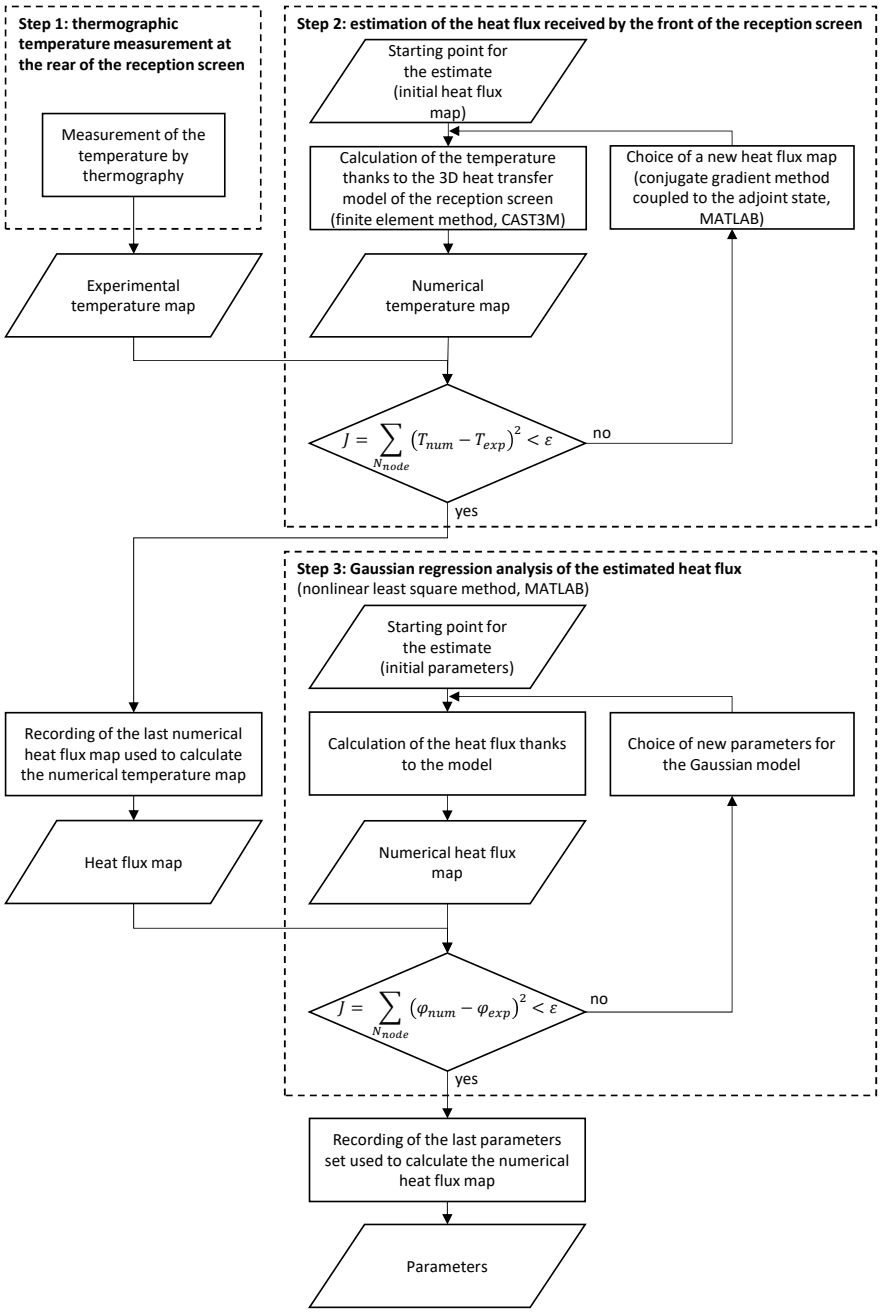

Figure 3: Flowchart describing the methodology.

2.3. Measuring tools

Solar direct normal irradiance is measured using a Kipp & Zonen RaZON+ PH1 pyrheliometer located on a nearby rooftop. It is recorded every minutes and the measurement uncertainty is estimated at 2 %.

The infrared camera used for the measurements is of reference Telops FAST M3K. This camera works in the infrared range from 3.0 µm to 5.5 µm. It is equipped with a filter wheel containing one empty slot and three neutral-density filters (therefore four positions in total) and is able to realise multi integration times acquisitions. Thus, it is calibrated over a wide temperature range going from 0 °C to 1500 °C. To obtain accurate measurements over the temperature range expected here, 50 °C to 500 °C, the three first filter wheel positions and four integration times per position are used. The camera provides an image of 320 x 256 pixels. In the test-bench configuration, it is used with a 13 mm lens and provides a pixel size projected on the cast-iron plate of about 3.5 x 3.5 mm^2.

As mentioned earlier, a screen is used as interface between the reflector and the infrared camera. This screen is a lamellar graphite cast-iron plate (JL200) 1 m long, 0.6 m high and 13 mm thick.

When using an infrared camera without additional direct temperature measurement, it is necessary to know the emissivity of the observed surface. In addition, measurements are made easier if this emissivity is stable over time and homogeneous over the surface. For this reason, the surface of the plate observed by the infrared camera was painted with the special high-temperature paint Pyromark 2500 from LA-CO Industries. The application process is described in Appendix B.

The air temperature is measured out of direct sunlight at a frequency of 1 Hz using 1.5 mm thick K-type thermocouples and a Lutron BTM-4208SD data-logger. Wind speed is measured near the test bed at a frequency of 1 Hz with a Davis 7911 anemometer connected to an electronic board (Arduino Uno). The method used to process the experimental data is given in Appendix A.

2.4. Experimental protocol

To begin with, the system is set up in a place exposed to the sun and without any shadows to interfere with the experiment. During the entire experiment, the cast iron plate and the measuring instruments are protected from direct sunlight in order to avoid reflection of direct sunlight from the plate onto the camera and to avoid overheating of the electronics.

Then the Scheffler reflector is briefly turned towards the sun to establish its curvature and measure its angle to the vertical. Once this is done, the wind and ambient temperature start to be recorded; the normal direct irradiance is continuously recorded by the weather station. The Scheffler is turned again towards the sun and the sun tracking system is activated.

When steady state is reached, several measurements are taken with the infrared camera around solar noon at regular intervals. For each one of these measurements, a short video (approximately 400 frames at 20 Hz) is recorded with each filter and with multi-integration times. The conditions are assumed to remain stable during the recording period, *i.e.* a bit less than 10 min. Then an average image combining all those recorded is saved. This allows reducing the measurement noise and catching the full range of temperatures observed.

Finally, the reflector is turned away from the sun and every recording is stopped.

2.5. Heat flux collected

The total intensity of the heat flux collected by a Scheffler reflector [18] depends on its aperture area, denoted $A_{ap,\,n}$, and on the direct normal irradiance (DNI), denoted I (obtained experimentally with the pyrheliometer). This gives:

$$\dot{Q}_{in} = A_{ap,\,n} \cdot I. \tag{1}$$

The aperture area $A_{ap,\,n}$ is lower than the effective collector area A_{ef} and varies with the Sun's declination δ_n of the n^{th} day of the year and can be calculated for the northern hemisphere as defined by (2) [4].

$$A_{ap,\,n} = \eta_{cov} \cdot A \cdot \cos\left(\zeta + \frac{\delta_n}{2}\right). \tag{2}$$

For the southern hemisphere, the addition within the cosine simply becomes a subtraction. The section plane angle ζ is a construction parameter of the reflector which represents the angle between the plane of the elliptic edge of the reflector and the sun rays at equinox. In the present case, its value is 43.23° [1]. By construction, the aperture area is constant over a day, but it should be noted that it varies by about 50 % between summer and winter [3].

Another approach to obtain the aperture is to experimentally measure the inclination of the plane of the elliptical edge of the reflector at solar noon

β with respect to the vertical. The aperture area can then be computed thanks to the sun elevation angle ξ at solar noon.

$$A_{ap,\,n} = \eta_{cov} \cdot A \cdot \cos(\xi - \beta). \tag{3}$$

In (3), the angle β from the vertical is counted as positive when the reflector faces the sky and negative when it faces the ground.

2.6. Heat flux delivered estimated by inverse method

In order to estimate the heat flux delivered by the Scheffler reflector, the cast-iron plate is represented by a three-dimensional thermal model whose conductivity depends on temperature. This non-linear model is studied in steady state with radiative and convective exchanges at its boundaries (Figure 4a). The main properties taken into account in the model are given in Table 1. Heat transfer inside the cast-iron slab is described thanks to the thermal conductivity.

To determine the heat exchange by radiation, the cast iron plate is assumed to be a grey body in a black body environment. The proportion of the incident concentrated solar heat flux that is absorbed by the cast iron plate is quantified by the solar absorptivity of cast-iron α_c. Heat exchanges between the plate and its environment are quantified by two emissivities, that of the cast iron ε_c and that of the of the paint ε_p. Several measurements were carried out to determine the absorptivity and the emissivities, and are described in Appendix C. It should be noted that because of the tent on one side and the reflector on the other, the cast iron plate can hardly "see" the sky. It therefore exchanges radiation with its immediate surroundings, which are considered to be at air temperature.

Estimating the solar heat flux density also necessitates estimating the heat exchange by convection. Open convection on a vertical plate with inhomogeneous temperature can be particularly complex. For this reason, there is no simple correlation appropriate to the experimental set-up. Another method was therefore used. It is assumed that convective heat exchange can be represented by a single coefficient h that is estimated for each measurement. It is obtained by iteration, adjusting it in the numerical model until the flux estimated by inverse techniques at the edges of the plate is equal to the vertical global irradiance.

With this model and knowing the incoming heat flux $\varphi(x, y)$, it is possible to determine the temperature $T(x, y, z)$ in any point $M(x, y, z)$ of the plate

Ω: this is the direct problem described by the following equations. One notes Γ_1 the boundary of the plate exposed to the solar concentrated heat flux and Γ_2 the boundary of the other side of the plate and the sides. Moreover, the vector $\vec{n}$ is defined as the normal to the surface a the point $M(x, y, z)$. Finally, to ease the comprehension, one notes the temperature $T(x, y, z) = T$, the thermal conductivity $\kappa(T) = \kappa$ and the heat flux density at the boundary exposed to concentrated heat flux $\varphi(x, y) = \varphi$.
Thus, for any M in Ω, there is:

$$\nabla \cdot (\kappa \cdot \nabla T) = 0. \tag{4}$$

For all M on Γ_1, the condition at this boundary is written:

$$-\kappa \cdot \frac{\partial T}{\partial n} = -\alpha_c \cdot \varphi + \varepsilon_c \cdot \sigma \cdot \left(T^4 - T_{env}^4\right) + h \cdot (T - T_{env}) \,. \tag{5}$$

For all M on Γ_2, the condition at this boundary is written:

$$-\kappa \cdot \frac{\partial T}{\partial n} = \varepsilon_p \cdot \sigma \cdot \left(T^4 - T_{env}^4\right) + h \cdot (T - T_{env}) \,. \tag{6}$$

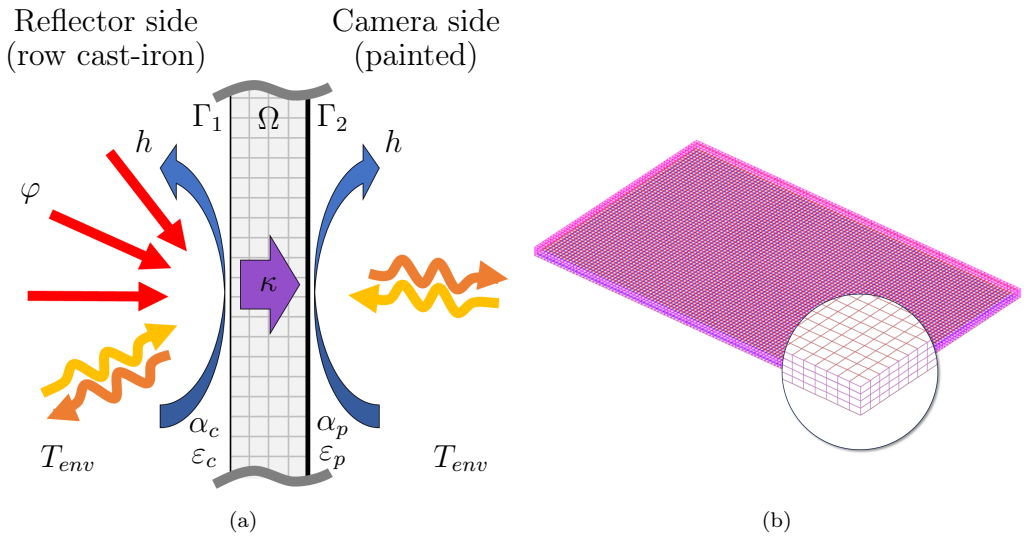

Figure 4: Side view of the receiver with the heat transfers (a) and mesh of the 3D model (b). The mesh consists of 24 000 cubic quadratic elements with 8 nodes: 100 in the length of the cast-iron slab (x-axis), 60 in its height (y-axis) and 4 in its thickness (z-axis).

Table 1: Material properties taken into account in the thermal model of cast iron. The solar absorptivity is the average of the monochromatic absorptivities between 0.25 µm and 2.5 µm weighted by the standard solar spectrum. Similarly, the spectral emissivity is the average of the monochromatic emissivities between 2.5 µm and 25 µm weighted by the emission spectrum of a black body of given temperature between the same wavelengths. The average spectral emissivity is then the average of the spectral emissivities obtained for blackbody temperatures between 50 °C and 500 °C. For more details, see Appendix C.

Property	Value
Thermal conductivity, κ ($\mathrm{W \cdot m^{-1} \cdot K^{-1}}$)	$\kappa = 49.85 - 0.0106 \cdot T$ [19] (T expressed in °C)
Solar absorptivity of cast-iron, α	0.88
Mean spectral emissivity of cast-iron, ε_c	0.77
Mean spectral emissivity of the paint, ε_p	0.77
Convective exchange coefficient, h ($\mathrm{W \cdot m^{-2} \cdot K^{-1}}$)	7

The direct problem is solved with the CAST3M software using the finite element method. The mesh consists of 24 000 cubic quadratic elements with 8 nodes: 100 in the length of the cast-iron slab (x-axis), 60 in its height (y-axis) and 4 in its thickness (z-axis).

The inverse problem is to determine the intensity and distribution of the concentrated heat flux absorbed on the reflector-side of the plate that causes the temperature measured on the camera-side of the plate. It is solved thanks to a minimisation based on the conjugate gradient method coupled with the adjoint state [17]. In other words, we estimate $\varphi(x, y)$ that minimises the cost function J, which is the sum of the squares of the differences between the experimental temperature and the numerical temperature:

$$J = \sum_{N_{node}} \left(T_{num} - T_{exp}\right)^2 . \tag{7}$$

In addition to the heat flux density map obtained, the total intensity of the heat flux delivered by the reflector $\dot{Q}_{out}$ can be calculated as:

$$\dot{Q}_{out} = \int_{A_{abs}} \varphi(x, y)\, dA_{abs}, \tag{8}$$

with A_{abs} the surface area of the cast iron plate observed by the infrared camera. It is assumed that the radiative heat flux coming from the environment is negligible compared to that delivered by the reflector.

The total intensity of the heat flux delivered can be compared with the theoretical one. Indeed, (9) shows that the theoretical total intensity of the heat flux delivered $Q_{out,\,th}$ can be estimated from the heat flux collected $\dot{Q}_{in}$, the specular reflectivity of the mirrors ρ_{spec} and the proportion of the rays collected by the reflector which reach the target γ, *i.e.* the intercept factor of the screen.

$$\dot{Q}_{out,\,th} = \rho_{spec} \cdot \gamma \cdot \dot{Q}_{in}. \tag{9}$$

The specular reflectivity of the mirrors is assumed to be close to the global reflectivity of the mirrors. And as the measurement interface is big and should thus collect most of the concentrated heat flux, the value of the intercept factor γ is expected to be close to 100 %.

Before continuing, it should be noted that a crack appeared in the cast-iron slab before the measurements on 14 June 2022. This crack, visible on Figure 5, is probably due to the high temperature gradient in the plate. Its effect on heat conduction is not taken into account in the numerical thermal model and will be discussed in Sections 3.2 and 3.3. Another cast-iron plate without crack is used for the experiments on 22 March 2023 and 20 April 2023.

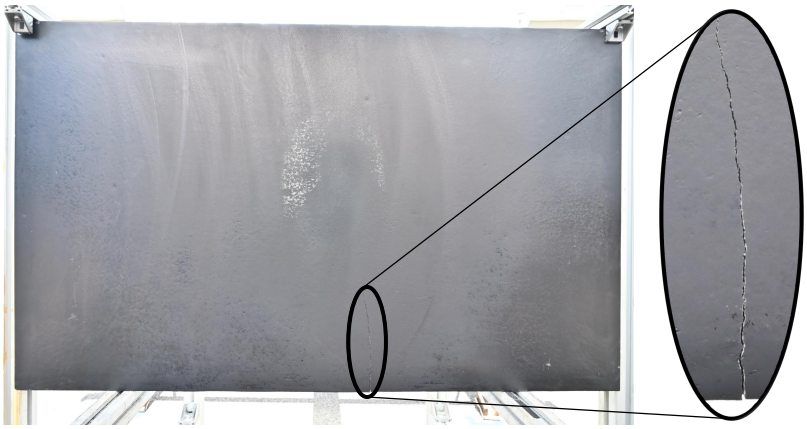

Figure 5: Visual aspect of the painted face of the first cast-iron slab. A crack appeared in a previous heating cycle.

2.7. Variables of interest

The key quantities in this work are the density and total intensity of the heat flux supplied as well as the shape and size of the heat flux distribution. But to make it easier to compare results with other works, they are transformed into dimensionless quantities.

As first dimensionless performance indicator, the total heat flux delivered by the Scheffler reflector $\dot{Q}_{out}$ can be compared with the heat flux collected $\dot{Q}_{in}$, as shows (10), to obtain the experimental energy efficiency η_{ref} of the reflector.

$$\eta_{ref} = \frac{\dot{Q}_{out}}{\dot{Q}_{in}}. \tag{10}$$

It should be noted that the term "optical efficiency", often denoted η_o, usually refers to the efficiency of the optical part of a system (such as a solar cooker) and therefore includes the reflectivity of a possible secondary mirror, the transmissivity of a possible transparent cover on the absorber and the absorptivity of the absorber. As this work intends to go into more detail in the performance analysis of the Scheffler reflector, the latter is studied without any secondary optics and the output power is defined as the power received, and not absorbed, by the flat vertical screen located in the focal area. In this way, the calculated energy efficiency gives information about the reflector only, and thus allows comparison between different reflectors independently from the absorber and any intermediate optical object.

Another important characteristic of a reflector is its concentration ratio. The concentration ratio has several definitions, all of which have their advantages and disadvantages [20, 21]. In the present case, the characteristics of the reflector are studied without any *a priori* on the absorber size. That is why the area concentration ratio is defined by:

$$C_a = \frac{A_{ap,\,n}}{A_{i,\,n}}. \tag{11}$$

This ratio compares the aperture area of the reflector $A_{ap,\,n}$ with the area of the image $A_{i,\,n}$ produced in the focal zone of the reflector (*e.g.* on a measurement screen). Note that, as $A_{ap,\,n}$ varies through the year, C_a is also expected to vary. Knowing the value of the area concentration ratio throughout the year enables the absorber to be designed accordingly and a detailed performance analysis to be carried out. In addition, this concentration ratio can be measured regularly over the lifetime of the reflector and used to assess the

loss of concentration due to reflector ageing.

Energy efficiency is an energy indicator and the surface concentration ratio is a geometric indicator. It is also interesting to have other quantities which combine these to aspects. The average heat flux density concentration ratio $C_{f,av}$ is defined by (12).

$$C_{f,\,av} = \frac{\dot{Q}_{out}}{A_{i,\,n} \cdot I}. \tag{12}$$

This latter indicator gives a measure of the reflector's performance in simultaneously transmitting and concentrating solar energy.

Now that the performance indicators are defined, the results can be presented.

3. Results and Discussion

3.1. First results and observations

The experiments took place in Marseille, France (lon. 5.4374° E, lat. 43.3449° N), on 14 June 2022, 22 March 2023 and 20 April 2023. As the analysis procedure is the same for all the measurements, one measurement is first described in detail, then the results of the other measurements are briefly presented and compared.

Thus, this section mainly describes the measurement 3 on 14 June 2022. It was realised close to solar noon (11:57), a few days before the June solstice (northern hemisphere). That day, the intercept area of the reflector $A_{ap,\,165}$ was $4.3\,\mathrm{m}^2 \pm 0.2\,\mathrm{m}^2$. The average direct normal irradiance during this measurement was $904\,\mathrm{W} \cdot \mathrm{m}^{-2}$ with a standard deviation of $0.7\,\mathrm{W} \cdot \mathrm{m}^{-2}$ (k = 1).

The following graphs are drawn from the point of view of the infrared camera, the x-axis being horizontal (length of the cast-iron slab), the y-axis being vertical (height) and the z-axis coming from the cast-iron slab to the camera (thickness).

3.2. Experimental temperature field

Figure 6 shows the temperature measurement at the camera-side of the cast-iron slab. As the emissivity of the surface has been taken into account, these temperatures are expressed as "true temperatures", by opposition to "black body temperatures".

From a qualitative point of view, one can see a hot spot at the middle and a temperature gradient from this point to the edges of the plate. The isothermal lines appear almost circular. On the picture, a small defect is visible at the bottom of the plate: this is a temperature discontinuity due to the narrow crack which appeared before our measurement. Its influence on the heat flux estimate is discussed in Section 3.3. In addition, the fact that there is no other temperature discontinuity confirms the hypothesis of a homogeneous emissivity despite the visual aspect of the screen (5). From a quantitative point of view, the temperature varies from 45 °C at the edges, to 486 °C ± 5 °C in the middle.

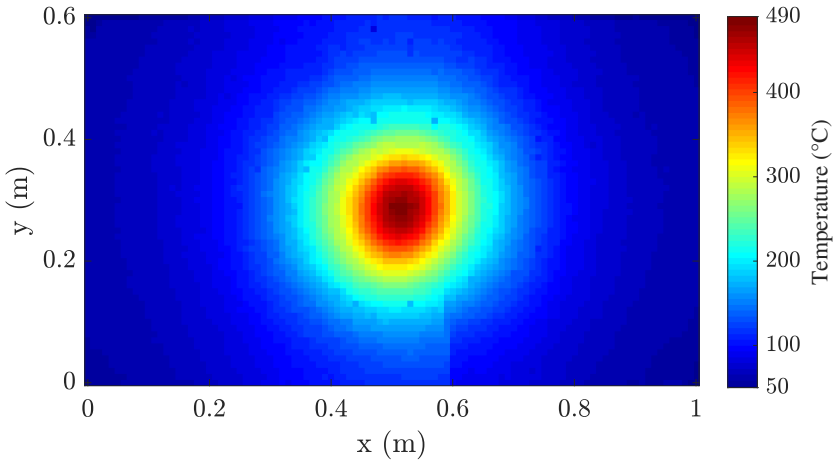

Figure 6: Experimental temperature field obtained with the infrared camera and after treatment with emissivity.

3.3. Experimental heat flux intensity and distribution

As explained in Section 2, the received heat flux is estimated from the temperature measurements using inverse techniques. Figure 7 represents the heat flux density received by the cast-iron slab. This figure shows that the use of an infrared camera in combination with the inverse techniques represents a relevant solution to access the whole heat flux distribution with a good resolution.

The heat flux distribution shape is similar but narrower than the temperature one. The estimation of the heat flux density generated a small "wave" near the location of the crack. This non-physical phenomenon is partly due to our model and to inverse techniques, which do not take the crack into

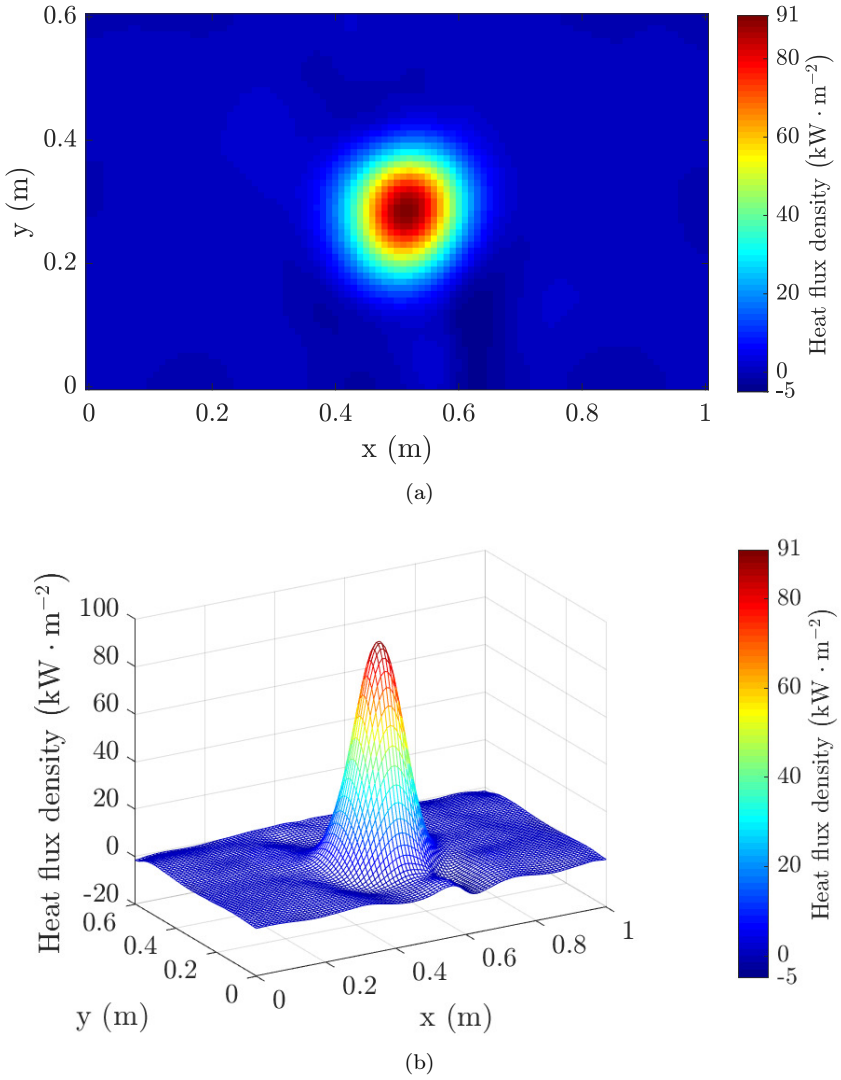

Figure 7: Experimental heat flux map in a 2D representation (a) and in a 3D representation (b). The heat flux density varies from $-5\,\mathrm{kW \cdot m^{-2}}$ (numerical artefact) to $91\,\mathrm{kW \cdot m^{-2}}$ and gives a total heat flux received by the cast-iron plate equal to 2.5 kW.

consideration. But this is only a local issue and global results are visually not much affected. This demonstrates the robustness of the method, even in an unfavourable case. Another measurement carried out using a screen without crack is showed in Appendix D.

The heat flux density reaches a maximum of $91\,\mathrm{kW \cdot m^{-2}} \pm 9\,\mathrm{kW \cdot m^{-2}}$

and the total intensity of the heat flux received by the cast-iron plate is $2.5\,\mathrm{kW} \pm 0.2\,\mathrm{kW}$.

The surface of the cast iron plate exposed to the concentrated solar heat flux also receives a diffuse solar heat flux, either directly or indirectly after reflection in the environment. As it represents around 4 % of the total heat flux, it is smaller than the uncertainty and is neglected in this work.

As the direct normal irradiance was $904\,\mathrm{W \cdot m^{-2}} \pm 9\,\mathrm{W \cdot m^{-2}}$ and the aperture of the Scheffler reflector was $4.3\,\mathrm{m^2} \pm 0.2\,\mathrm{m^2}$, the power received by the Scheffler reflector was $3.9\,\mathrm{kW} \pm 0.2\,\mathrm{kW}$. Thus, the efficiency of the Scheffler reflector to concentrate and transmit the solar radiation to the plate was $63\,\% \pm 6\,\%$.

The efficiency is a bit low compare to our expectations and measurement uncertainties do not explain the difference. Indeed, (9) and (10) give rise to (13).

$$\eta_{ref} = \rho_{spec} \cdot \gamma \tag{13}$$

Thus, either the specular reflectivity is below 80 % (i.e., below the value of the global reflectivity), or the intercept factor is below 100 %, or both. Given the large size of the receiving screen and the fact that there is no visible "sunlight leakage", the first explanation is privileged: the mirrors are not perfectly specular and scatter the sunlight.

Despite this last point, these results are in good agreement with those of Oelher and Scheffler [3]. The latter carried out measurements in April using an $8\,\mathrm{m^2}$ reflector. With an aperture of $4.7\,\mathrm{m^2}$ (8 % bigger) and a direct normal irradiance of $730\,\mathrm{W \cdot m^{-2}}$ (19 % smaller), they obtained a total heat flux of 2.1 kW (15 % smaller), giving an efficiency of 61 % (only 2 % smaller than ours).

However, the results are significantly different from those of Sasidharan and Dutta [14]. They studied a reflector four times bigger (area of $32.0\,\mathrm{m^2}$ and aperture estimated to $27.1\,\mathrm{m^2}$) and with a direct normal irradiance of $651\,\mathrm{W \cdot m^{-2}}$ (28 % smaller), they obtained a total heat flux of only 860 W (65 % smaller). Moreover, the maximum heat flux density is $45\,\mathrm{kW \cdot m^{-2}}$ (two times smaller), and they have a nearly random heat-flux distribution whereas Figure 7 shows a very typical distribution. There are several possible explanations for this. Firstly, a $32\,\mathrm{m^2}$ Scheffler reflector is further away from the focal point and more difficult to build than an $8\,\mathrm{m^2}$ reflector, therefore the heat flux may be more distributed due to shape defects. Secondly, as the curvature of the reflector is adjusted manually, this could be due to

inaccurate adjustment. Finally, as they used only 5 heat flux sensors, they needed a hybrid experimental-numerical technique to reconstruct the heat flux distribution, which led to significant assumptions, especially in the ray-tracing model. In contrast, the measurement technique described in Section 2 uses an infrared camera to provide a spatially resolved measurement over the entire surface of the receiving screen. It therefore requires very few assumptions to give a detailed description of the phenomenon. For the above reasons, the experimental results of Sasidharan and Dutta cannot therefore be used to validate or invalidate the present results.

On the other hand, our results are fairly consistent with those of Dib [16]. He carried out a measurement with a $2.7\,\mathrm{m}^2$ Scheffler reflector on 8 December in the southern hemisphere, a date roughly comparable to the June solstice in the northern hemisphere. With an aperture of $1.3\,\mathrm{m}^2$ (71 % smaller) and under a direct normal irradiance of $996\,\mathrm{W}\cdot\mathrm{m}^{-2}$ (10 % bigger), he measured a total heat flux of 1.3 kW (49 % smaller) and heat flux densities up to $299\,\mathrm{kW}\cdot\mathrm{m}^{-2}$ (229 % bigger). It should be noted that the latter two results could be overestimated. Indeed, the total heat flux seem to be calculated from the aperture and the direct normal irradiance neglecting the reflectivity of the mirrors (about 90 %), and the heat flux densities are estimated on the basis of this total flux and the grey scale map obtained with a CMOS camera. Nevertheless, once again, a bigger reflector generally implies a more distributed heat flux. Moreover, Dib's reflector is covered by an aluminium reflective film which stick to the parabolic structure, whereas the present reflector is covered with flat glass mirrors; the concentration and the heat flux densities are thus more limited in the present case than in Dib's case (see the work of Reddy and Khan [6]).

Dib also gave information on the size of the heat flux distribution. Nevertheless, it appears that determining the contour of the distribution is not an easy task and may be subjective because the boundaries are not clear. Instead of arbitrarily setting a heat flux threshold that would define the distribution boundary, we decided to choose a model and fit it to the experimental data in order to provide more objective and quantitative information on the heat flux distribution.

3.4. Heat flux distribution model

As the heat flux distribution seems to behave like a two-dimensional Gaussian curve, a regression analysis is performed accordingly. The chosen regres-

sion function model is:

$$\varphi(x,y) = \varphi_{max} \exp\left(-a(x-x_c)^2 - 2b(x-x_c)(y-y_c) - c(y-y_c)^2\right) + \varphi_{offset} \tag{14}$$

with $a = \frac{\cos^2(\theta)}{2\sigma_{x1}^2} + \frac{\sin^2(\theta)}{2\sigma_{y1}^2}$, $\quad b = +\frac{\sin(2\theta)}{4\sigma_{x1}^2} - \frac{\sin(2\theta)}{4\sigma_{y1}^2}$, $\quad$ and $c = \frac{\sin^2(\theta)}{2\sigma_{x1}^2} + \frac{\cos^2(\theta)}{2\sigma_{y1}^2}$.

The maximum of the Gaussian curve is denoted φ_{max}. It can also be written as the product of the the direct normal irradiance and the maximum local flux concentration ratio. The two-dimension curve is centred on the position (x_c, y_c) and spreads along its two axes according to the standard deviation σ_{x1} and σ_{y1}. The angle θ describes the angle between the reference frame $(O, \mathbf{e}_x, \mathbf{e}_y, \mathbf{e}_\varphi)$ and the frame of the Gaussian curve $(C, \mathbf{e}_{x1}, \mathbf{e}_{y1}, \mathbf{e}_\varphi)$. It rotates the Gaussian curve in the trigonometric direction as it increases. And the last parameter φ_{offset} is the heat flux offset due to the vertical global irradiance received by the cast-iron plate from the environment.

The estimation of the parameters was realised with a non linear least square minimisation on MATLAB. The minimisation appeared to converge rapidly and to be robust against the start point and bounds. The estimated parameters of the model for the measurement 3 on 14 June 2022 are presented in Table 2.

Table 2: Parameters of the Gaussian function model estimated for the measurement 3 of the experiment carried out on 14 June 2022. Parameters are: the maximum heat flux density (φ_{max}), the heat flux density offset due to global vertical irradiance (φ_{offset}), the position of the centre (x_c, y_c), two standard deviations (σ_x, σ_y) and the rotation angle (θ).

Parameter	Value
φ_{max} ($\mathrm{kW \cdot m^{-2}}$)	93.5
φ_{offset} ($\mathrm{kW \cdot m^{-2}}$)	0.3
x_c (mm)	514
y_c (mm)	284
σ_{x1} (mm)	66
σ_{y1} (mm)	60
θ (°)	60

A comparison between the third experimental heat flux measurement and the Gaussian model is given on Figure 8 (Gaussian curve with 2 axes), Figure 9a (axis (Cx_1)) and Figure 9b (axis (Cy_1)). A good match can be observed on all figures and the residuals are signed but remain small compare

to the heat flux received in the middle of the cast-iron plate. It can be noted that the peak of the experimental heat flux distribution is slightly flattened compared to the model. This could be partly due to the flat facets of the reflector. Indeed, a reflector with smaller facets should theoretically achieve higher heat flux densities, and would fit the model better. Nevertheless, the model gives an estimated maximum density only 3 % greater. If the experimental distribution is not exactly a Gaussian curve, it is still a very good approximation. Moreover, as the value of the first deviation (σ_x) remains 10 % lower than that of the second (σ_y), the experimental distribution is closer to a two-dimensional Gaussian curve than to a one-dimensional Gaussian curve. Finally, the centre of the Gaussian curve is close to the middle of the cast iron plate, *i.e.* where the focal point is supposed to be (with an accuracy estimated to ±5 cm in each direction).

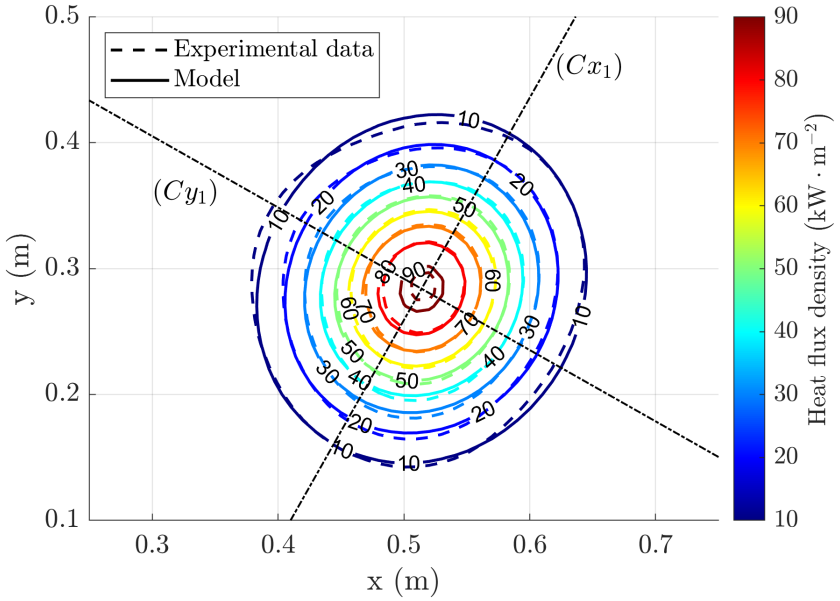

Figure 8: Experimental heat flux distribution versus fitted function. The two dotted lines represent the axes (Cx_1) and (Cy_1) of the Gaussian regression function.

The model fits the experimental data very well, so it is reasonable to use it to describe the heat flux distribution quantitatively. In order to compare the present results with other works, in which authors often consider the contour containing about 100 % of the heat flux, a coverage factor k of 3 was chosen, thus defining an ellipse containing 99.7 % of the heat flux. Thus,

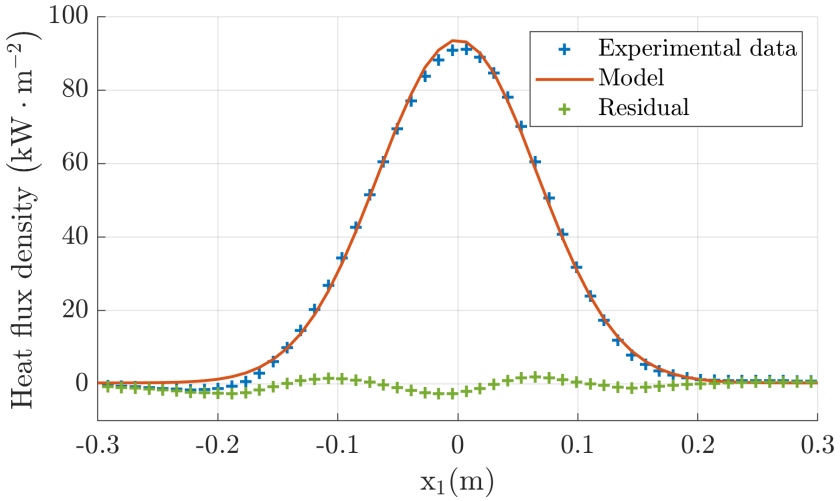

(a)

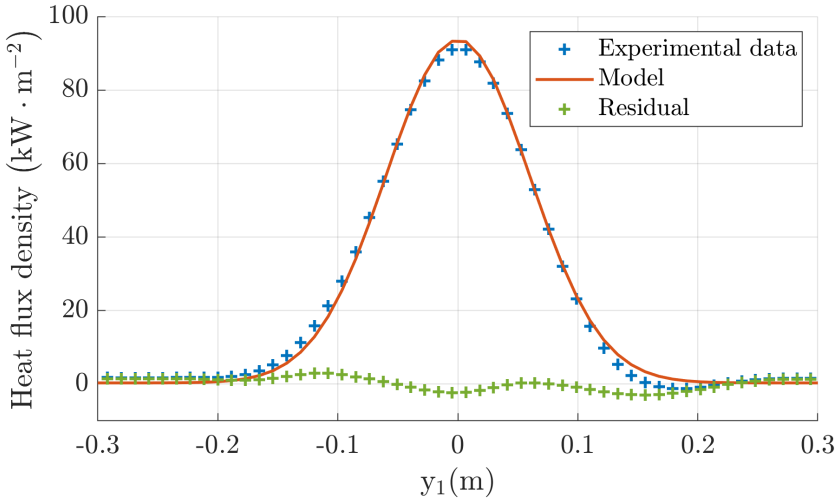

(b)

Figure 9: Experimental data versus model data according to (Cx_1) axis (a) and (Cy_1) axis (b)

the major and minor axes (or major and minor widths) of this ellipse are calculated with:

$$W_{x_1,\,99.7\%} = 2 \cdot k_{99.7\%} \cdot \sigma_{x1} \quad \text{and} \quad W_{y_1,\,99.7\%} = 2 \cdot k_{99.7\%} \cdot \sigma_{y1}. \tag{15}$$

This gives respectively 0.399 m and 0.358 m, and the surface area covered

by the heat flux distribution, called image area, is thus $0.112\,\mathrm{m}^2$. As a direct consequence, the area concentration ratio of the reflector is 39 and the average flux concentration ratio is 24. Firstly, it can be seen that the surface is consistent with the idea that the spot can never be smaller than the size of a mirror of the parabola. Secondly, it can be assumed that misalignment and scattering are responsible for the larger size of the spot.

These experimental results can now be compared with those of Dib [16]. He also assumed the heat flux distribution to be elliptical and found major and minor axes of 0.347 m and 0.286 m respectively. This results in an image area of $0.078\,\mathrm{m}^2$, *i.e.* 30 % smaller. This comparison corroborates the results, as it is consistent with the explanations given in Section 3.3: Dib's reflector has a shorter focal length and provides higher heat flux densities than ours due to a narrower heat flux distribution, even though the total heat flux is lower.

In summary, the comparison between the current results and the literature shows a satisfactory agreement, thus validating the method and the results.

3.5. Measurement repeatability and evolution with time

Now that a measurement has been analysed in detail, the results of the measurements can be studied more globally. The measurement results are summarised in Tables 3, 4 and 5. In what follows, all the measurements are taken into account with the exception of the last two on 22 March 2023, which were affected by a failure in the tracking system (it is particularly visible in the coordinates of the maximum of the Gaussian curve).

Among the performance indicators calculated, energy efficiency is an indicator that should not change depending on the time of day or the day of the year. The average energy efficiency of all the data is 64 %, with a standard deviation of 2 % and a range of 6.5 %, while the uncertainty is estimated at ±6 %. Variability in energy efficiency is therefore relatively low and could be attributed to the uncertainty of the measurements. So far, the measurements appear to be fairly repeatable.

Note that although the method has good repeatability (variations slightly less than the uncertainties), it may not be easily reproducible due to its complexity. In addition, the performance characteristics of Scheffler reflectors may also vary considerably due to the lack of standardisation in their design and use. Thus, other methods such as the use of a cooled Lambertian screen and flow sensors would suffer from similar limitations.

Table 3: Data of the experiment of the 14 June 2022.

General information				
Date (dd/mm/yyyy)			14/06/2022	
Solar time (hh:mm)	11:14	11:32	11:57	12:52
Aperture (m^2)			4.3	
Environment data				
DNI ($W \cdot m^{-2}$)	900	902	904	907
Air temperature (°C)	29.5	28.9	30.2	31.2
Wind velocity ($m \cdot s^{-1}$)	0.5	1.0	0.9	0.5
Experimental data (thermography and inverse techniques)				
Max. temperature (°C)	474	476	486	485
Max. heat flux ($kW \cdot m^{-2}$)	90.8	81.1	91.1	92.9
Tot. heat flux (kW)	2.4	2.4	2.5	2.5
Efficiency (%)	61	61	63	63
Estimated parameters (two-dimensional Gaussian model)				
φ_{max} ($kW \cdot m^{-2}$)	93.2	82.6	93.5	95.4
φ_{offset} ($kW \cdot m^{-2}$)	0.3	0.1	0.3	0.3
x_c (mm)	517	515	514	508
y_c (mm)	275	278	284	297
σ_{x1} (mm)	65	69	66	69
σ_{y1} (mm)	60	65	60	58
θ (°)	72	64	60	60
Deduced data (ellipse containing 99.7 % of the heat flux)				
Major diameter (m)	0.389	0.416	0.398	0.413
Minor diameter (m)	0.359	0.390	0.358	0.346
Image area (m^2)	0.110	0.128	0.112	0.112
Area C.R.	40	34	39	39
Average flux C.R.	24	20	24	24

Table 4: Data of the experiment of the 22 March 2023.

General information								
Date (dd/mm/yyyy)	22/03/2023							
Solar time (hh:mm)	11:06	12:04	12:43	13:07	13:33	14:02	14:33*	15:05*
Aperture (m^2)	5.5							
Environment data								
DNI ($W \cdot m^{-2}$)	862	876	886	885	873	861	838	804
Air temperature (°C)	18.1	18.8	19.2	20.1	19.9	19.8	20.0	19.9
Wind velocity ($m \cdot s^{-1}$)	0.3	0.5	0.7	0.3	0.4	0.5	0.4	0.4
Experimental data (thermography and inverse techniques)								
Max. temperature (°C)	483	472	469	471	463	460	372	436
Max. heat flux ($kW \cdot m^{-2}$)	109.2	111.0	96.2	105.9	98.5	91.2	54.8	86.5
Tot. heat flux (kW)	2.9	3.1	3.2	3.2	3.2	3.2	3.1	3.1
Efficiency (%)	62	64	65	65	67	67	67	70
Estimated parameters (two-dimensional Gaussian model)								
φ_{max} ($kW \cdot m^{-2}$)	109.3	111.2	95.3	105.4	97.0	90.0	54.9	85.7
φ_{offset} ($kW \cdot m^{-2}$)	−0.2	0.4	0.3	0.4	0.4	0.3	0.3	0.6
x_c (mm)	488	492	499	503	505	502	583	518
y_c (mm)	255	277	286	291	302	310	380	340
σ_{x1} (mm)	71	71	81	78	83	87	119	89
σ_{y1} (mm)	65	59	64	59	60	62	75	59
θ (°)	84	71	73	73	76	80	80	83
Deduced data (ellipse containing 99.7 % of the heat flux)								
Major diameter (m)	0.424	0.424	0.484	0.465	0.498	0.521	0.711	0.533
Minor diameter (m)	0.387	0.354	0.382	0.351	0.361	0.372	0.449	0.354
Image area (m^2)	0.129	0.118	0.145	0.128	0.141	0.152	0.251	0.148
Area C.R.	43	46	38	43	39	36	22	37
Average flux C.R.	26	30	25	28	26	24	15	26

* Measurements which were affected by a failure of the sun tracking system.

Table 5: Data of the experiment of the 20 April 2023.

General information							
Date (dd/mm/yyyy)	20/04/2023						
Solar time (hh:mm)	11:02	11:33	12:01	12:30	13:00	13:30	14:21
Aperture (m^2)	5.0						
Environment data							
DNI ($W \cdot m^{-2}$)	911	911	913	922	926	903	897
Air temperature (°C)	19.1	19.7	20.4	20.2	20.0	20.3	20.4
Wind velocity ($m \cdot s^{-1}$)	0.4	0.4	0.5	1.0	1.4	0.8	1.1
Experimental data (thermography and inverse techniques)							
Max. temperature (°C)	461	460	460	460	458	453	450
Max. heat flux ($kW \cdot m^{-2}$)	98.7	109.7	111.7	104.6	92.3	96.1	96.4
Tot. heat flux (kW)	2.9	3.1	3.2	3.2	3.2	3.2	3.1
Efficiency (%)	61	63	64	64	63	65	66
Estimated parameters (two-dimensional Gaussian model)							
φ_{max} ($kW \cdot m^{-2}$)	103.6	116.6	118.8	109.8	95.9	100.1	99.9
φ_{offset} ($kW \cdot m^{-2}$)	−0.6	−0.4	−0.3	−0.2	−0.3	−0.3	−0.2
x_c (mm)	491	492	492	492	494	521	522
y_c (mm)	273	272	273	273	273	286	297
σ_{x1} (mm)	79	75	75	77	82	79	79
σ_{y1} (mm)	62	57	56	59	64	63	63
θ (°)	85	86	86	87	86	89	88
Deduced data (ellipse containing 99.7 % of the heat flux)							
Major diameter (m)	0.473	0.452	0.449	0.464	0.489	0.476	0.474
Minor diameter (m)	0.375	0.344	0.337	0.353	0.387	0.379	0.377
Image area (m^2)	0.139	0.122	0.119	0.129	0.148	0.142	0.141
Area C.R.	36	40	42	39	33	35	35
Average flux C.R.	22	25	27	25	21	23	23

Unlike the energy efficiency, the area concentration ratio and the average flux concentration ratio should vary from one day to the next, as they depend on the aperture area and the image area. The aperture area varies according to the day of the year, but what about the image area? Using the same definition as in the previous section, the image area corresponds to the area of the ellipse containing 99.7 % of the heat flux received. The mean image area is $0.130\,\mathrm{m}^2$ with a standard deviation of $0.014\,\mathrm{m}^2$. Its major and minor diameters are 0.454 m and 0.365 m respectively.

One can note that, on average, the major axis of the ellipse is 14 % smaller in June than in March or April. Current measurements do not explain this phenomenon and further measurements would be required to determine whether this is due to the measurement uncertainty (including the uncertainty with setting up the test bench) or whether there is a trend towards a decrease in the major axis from March to June. Potentially influential parameters are discussed in the Appendix E.

In the meantime, no trend towards daily or seasonal variation can be identified for the image area and its axes, and the image area can be used to give a good order of magnitude for the average area concentration ratio, which is 39, and the average heat flux concentration ratio, which is 25.

4. Conclusion and perspectives

This paper presents measurements of the distribution of the concentrated heat flux delivered by an $8\,\mathrm{m}^2$ Scheffler reflector. Using an infrared camera and inverse techniques, a detailed map of heat flux densities is obtained without any *a priori*. The maximum heat flux density, total heat flux and energy efficiency are given with a relatively low uncertainty ranging from 6 % to 10 % and are in satisfactory agreement with the literature, confirming the relevance of the method.

Then, the experimental heat flux distributions are successfully compared with a model based on a two-dimensional Gaussian function. The estimated parameters allow a more detailed analysis of the experimental data and, in particular, provide quantitative data on the size of the heat flux distribution without the need for an arbitrary threshold.

The variation of the image area according to the time of the day or the day of the year appears to be of the same order of magnitude than the variability observed through the different experiments. This prevents an analysis of the variation of the variables of interest according to time. In average, 99.7 %

of the heat flux provided by the $8\,m^2$ is received on the vertical screen in an ellipse of major and minor diameters 45 cm and 37 cm respectively. And the area concentration ratio and heat flux concentration ratio are evaluated respectively to 39 and 25.

In future work, the data set on the performance of the Scheffler reflector should be supplemented by other experiments carried out at other times of day and on other days of the year. This would enable us to see more precisely how the characteristics of the heat flux supplied by the reflector vary as a function of time. Experiments could even be carried out with different sizes of reflector, different sizes of mirror, different inclinations of receiver, and so on. Furthermore, the diversity of experimental, theoretical and simulation results shows that there is a lack of experimental method and data to determine the most influential parameters and their values. Thus, such a data set could be useful for building accurate numerical models. In the meantime, these results already provide fundamental information for designers. Depending on the thermal characteristics of the absorber and the heat flow distribution characteristics, it is already possible to determine the absorber size that minimises heat loss.

5. Declaration of Interest

The authors declare that they have no known competing financial interests or personal relationships that could have appeared to influence the work reported in this paper.

6. Fundings

This work was supported by the Region Provence-Alpes-Côte d'Azur and the company Le Présage as part of the "Emplois Jeunes Doctorants" scheme. It was also supported by the Institute of Mechanics and Engineering of Aix-Marseille University. None of these funding sources were involved in study design; in the collection, analysis and interpretation of data; in the writing of the report; and in the decision to submit the article for publication.

7. Acknowledgments

The authors thank Nathalie Ehret, Yann Anquetin, Christophe Escape and Sadi Noël for their technical support.

8. Credit Author Statement

Gabriel Guillet: conceptualisation, methodology, validation, formal analysis, investigation, writing (original draft), visualisation, project administration
Jonathan Gaspar: methodology, software, validation, formal analysis, investigation, writing (review and editing)
Séverine Barbosa: conceptualisation, methodology, investigation, writing (review and editing), supervision, project administration, funding acquisition
Thomas Fasquelle: conceptualisation, methodology, investigation, writing (original draft, review and editing), supervision, project administration, funding acquisition
Benjamin Kadoch: conceptualisation, methodology, software, writing (review and editing), supervision, project administration, funding acquisition

Appendix A. Meteorological data processing

The meteorological data was processed according to the guidelines of the World Meteorological Organization.

Appendix A.1. Temperature

The air temperature is measured out of direct sunlight at a frequency of 1 Hz using 1.5 mm thick K-type thermocouples and a Lutron BTM-4208SD data-logger. In order to smooth the experimental data, a moving average is calculated at each second over a centred window of 1 min. The average and standard deviation of the temperature over each measurement duration is calculated based on this processed data.

Appendix A.2. Wind

Wind speed is measured with a Davis 7911 anemometer connected to an electronic board (Arduino Uno). The wind velocity is recorded at a frequency of 1 Hz. In order to smooth the experimental data, a moving average is calculated at each second over a centred window of 3 s (characteristic time of a gust of wind). The average and standard deviation of the wind velocity over each measurement duration is calculated based on this processed data.

Appendix A.3. Solar irradiance

Solar direct normal irradiance (DNI) is measured using a Kipp & Zonen RaZON+ SHP1-A pyrheliometer. It is recorded every minutes and the measurement uncertainty is estimated at 2 %. The average DNI over each measurement duration is calculated based on this data.

Appendix B. Paint application

The surface of the plate observed by the infrared camera was painted with the special high-temperature paint Pyromark 2500 from LA-CO Industries.

It was applied to the ground face of the cast iron slab using a short nap paint roller, after cleaning with sandpaper and acetone. It was left to dry for 63 h, and was then heated for an hour using a gaz-fired radiant panel; it reached 300 °C at the middle and 200 °C on the edges. The plate was subjected to three heating cycles prior to this study. The paint flaked slightly near the centre of the plate during the 2$^{\text{nd}}$ cycle. However, its condition appears to have remained stable during subsequent cycles.

Concerning the characteristics of the paint, Ho *et al.* [22] have shown that the substrate to which the paint is applied has an impact on its final emissivity. In addition, Coventry and Burge [23] and Caron *et al.* [24] have respectively shown that the final emissivity of the paint also depends on the painting and curing procedures. For these reasons, complementary emissivity measurements were made and taken into account in the temperature calculation. Notably, these measurements showed that the emissivity is homogeneous on the surface of the plate despite the flaking paint.

Appendix C. Spectral emissivity and solar absorptivity estimation method

In order to estimate the solar absorptivity and the infrared emissivity of the cast iron plate, samples have been analysed by PROMES-CNRS laboratory (Odeillo, France), for a measurement of their monochromatic emissivities, then, by applying a weighted-average of the product of the emissivity and the Planck's law (for spectral emissivities) or the Sun's irradiance spectrum (for solar absorptivity), spectral values were obtained for the different bandwidths of interest.

Appendix C.1. Monochromatic emissivity measurement method

Using a variable monochromatic light source, the samples were illuminated with a given angle of incidence θ and a given wavelength λ, then the hemispheric reflectivity was estimated using an integrating sphere and two different spectrophotometers, of which the main information are given in Table C.6. This was repeated over the entire wavelength range covered by the instruments.

Table C.6: Main information about the two spectrophotometers that were used to estimate the monochromatic reflectivities of the cast iron samples

Spectrophotometer	Perkin Elmer Lambda 950	Nicolet FTIR
Wavelength range	0.150 µm - 3.3 µm	1.25 µm – 25 µm
Wavelength step	10 nm	variable (3 nm - 850 nm)
Absolute uncertainty	0.005 (k=2)	0.005 (k=2)

From this reflectivity, considering that the material is opaque and assuming Kirchhoff's law of thermal radiation, the monochromatic directional emissivity $\varepsilon(\lambda, \theta)$ and absorptivity $\alpha(\lambda, \theta)$ can be obtained, *c.f.* equation C.1

$$\alpha(\lambda, \theta) = \varepsilon(\lambda, \theta) = 1 - \sigma(\lambda, \theta) \tag{C.1}$$

While it is known that absorptivities and emissivities depend on direction angle [25], here they had to be assumed independent of θ.

Appendix C.2. Spectral emissivity

The estimated spectral emissivity is obtained by comparing the flux emitted by the sample, thus weighted by its monochromatic emissivities and a flux emitted by a black body at the same temperature, as illustrated in Figure C.10, equation C.2 and equation C.3.

$$\varepsilon(\lambda_{min} -> \lambda_{max}) = \frac{\int_{\lambda_{min}}^{\lambda_{max}} \varepsilon(\lambda) \cdot M(\lambda) \cdot d\lambda}{\int_{\lambda_{min}}^{\lambda_{max}} 1 \cdot M(\lambda) \cdot d\lambda} \tag{C.2}$$

$$M(\lambda) = \frac{2 \cdot \pi \cdot h \cdot c^2}{\lambda^5} \cdot \frac{1}{\exp(\frac{h \cdot c}{\lambda \cdot k_B \cdot T}) - 1} \tag{C.3}$$

Note that the limits of the integrals are set by the limitations of the spectrophotometer, *i.e.* $\lambda_{min} = 250\ nm$ and $\lambda_{max} = 25\ \mu m$ and this affects the uncertainties on the estimate.

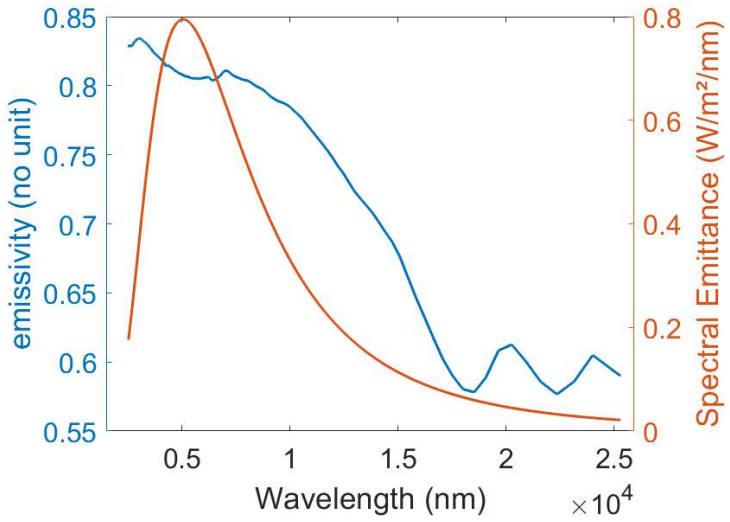

Figure C.10: Monochromatic emissivity of cast iron between 2.5 µm and 25 µm, and Planck spectrum of a black-body at 300 °C

Appendix C.3. Solar absorptivity: spectral emissivity for the range 250 nm - 2500 nm

The general equation for solar absorptivity that is estimated from the data is obtained by comparing a non-concentrated incident solar flux absorbed by the sample and the solar flux that would be absorbed by a black body, as shown in equation C.4 and Figure C.11.

$$\alpha_{solar} = \frac{\int_{\lambda_{min}}^{\lambda_{max}} I_{sun}(\lambda) \cdot \alpha(\lambda) \cdot d\lambda}{\int_{\lambda_{min}}^{\lambda_{max}} I_{sun}(\lambda) \cdot 1 \cdot d\lambda} \tag{C.4}$$

The solar spectral irradiance $I_{sun}(\lambda)$ are those of ASTM G-173-03, obtained through the NREL website.

Appendix C.4. Uncertainties

To estimate spectral emissivities/absorptivities, the integrations are performed over all the interval of wavelengths that is made possible by the spectrophotometers. However, taking the approximation that about 96 % of the spectrum's energy lays within $\lambda_{min} = \lambda(M_{max})/2$ and $\lambda_{min} = \lambda(M_{max}) \cdot 5$, with $\lambda(M_{max})$ the wavelength for which the emittance M is maximum, which

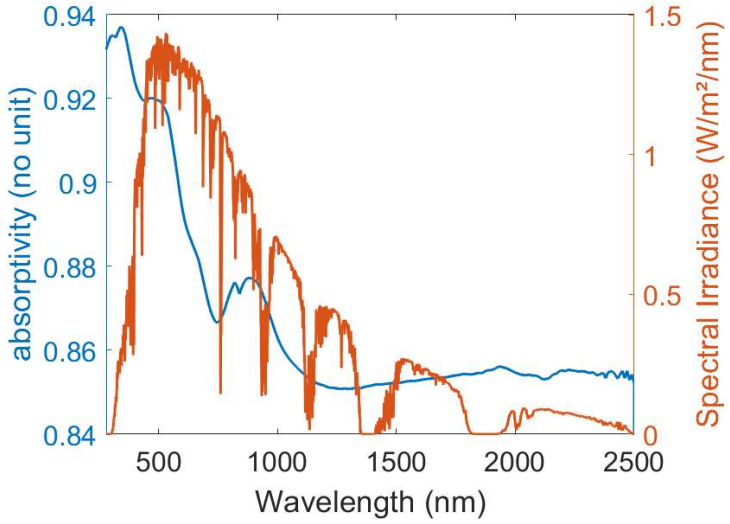

Figure C.11: Monochromatic emissivity/absorptivity of cast iron between 0.25 µm an 2.5 µm, ASTM G-173-03 solar spectrum

depends on the Wien constant and the temperature of the object, *c.f.* equation C.5,

$$\lambda(M_{max}) = \frac{\sigma_W}{T} = \frac{2.898 \cdot 10^{-3}}{T} \tag{C.5}$$

one can see that the spectral emissivity estimate for low temperatures will lack a non-negligible amount of data. The related uncertainty has therefore been set as the emittance difference between the black-body spectrum in the range of λ_{min} - λ_{max} and the emittance of the whole black-spectrum. Results vary between +2.7 % (@ 500 °C) and -16 % (@ 20 °C). Propagation from other uncertainties, *i.e.* deviation of the monochromatic emissivity measurements, differences between actual spectrums and reference ones, and directional dependence of emissivity, are difficult to estimate and are considered relatively negligible in comparison to these previous estimates, however, a 2 % relative uncertainty has been added to take them into account.

Appendix C.5. Results

The emissivity estimation has been performed for different blackbody temperatures, and results are gathered in Table C.7. It should be known that the effect of temperature, varied from ambient to 500 °C, on the monochromatic emissivity spectrums were negligible. Because the cast iron slab is

Table C.7: Spectral emissivity and absorptivity results.

T	20 °C	100 °C	200 °C	300 °C	400 °C	500 °C	5777K
$\lambda(M_{max})$ [µm]	9.89	7.77	6.13	5.06	4.31	3.75	0.50
$\lambda(M_{max})/2$ [µm]	4.95	3.89	3.06	2.53	2.15	1.88	0.250
$\lambda(M_{max}) \cdot 5$ [µm]	49.5	38.9	30.6	25.3	21.5	18.8	2.50
$\varepsilon(\lambda_{min} - \lambda_{max})$	0.71	0.74	0.76	0.78	0.79	0.80	0.88
$u(\varepsilon)$	-0.16/0.01	-0.10/0.02	-0.06/0.02	-0.04/0.02	-0.03/0.02	-0.03/0.02	-0.02/0.02

mainly above ambient and since the uncertainties on the values at low temperature are high, an average value of 0.77 +0.02/-0.05 has been chosen for the spectral emissivity. Note that his value should slightly vary across the slab but it has been set as constant for convenience.

Appendix D. Results of measure 1 of experiment 2

As indicated in Section 2.6, the crack in the receiver for the 14 June 2022 experiment is visible on the temperature map and causes a small wave on the heat flux map. A new receiver was used for the other two experiments. Taking the data from the first measurement carried out on 22 March 2023, the temperature map shows no discontinuity (Figure D.12) and the heat flux map shows "smoother" waves which are due to the numerical method (Figure D.13).

Appendix E. Influential parameters

The comparison between the current results and the literature shows that as soon as important parameters change, such as the size of the reflector or the date of the experiment, the experimental results differ considerably. Furthermore, the theoretical and numerical results also vary greatly depending on the assumptions made. This section therefore proposes an attempt to list the parameters influencing the results, to evaluate the limitations of the measurement method.

The size and shape of the heat flux distribution seem to have three main origins: the width of the sun, the intrinsic characteristics (or design features) of the reflector, and the reflection errors due to material manufacturing and installation. Firstly, the width of the sun implies that the sunlight arrives and is reflected in a cone. Secondly, reflector characteristics such as the size

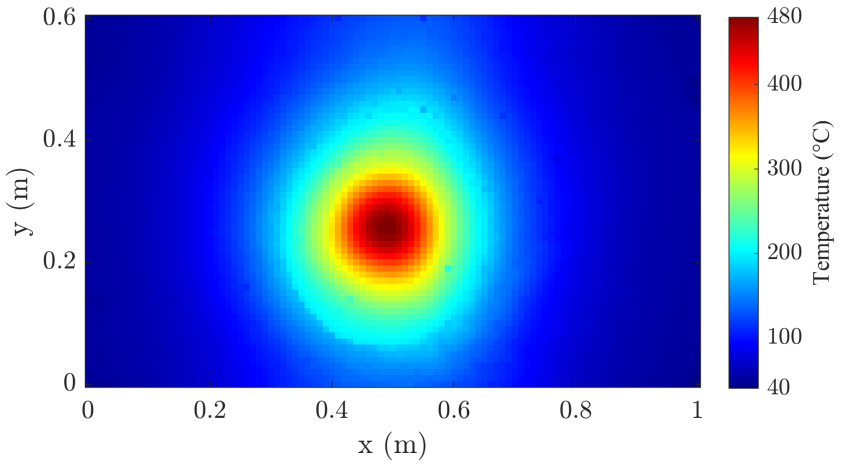

Figure D.12: Experimental temperature field obtained with the infrared camera for the first measurement on 22 March 2023.

of the mirrors, its focal length, and its tilt with respect to the declination of the Sun impact the size of the heat flux distribution (without changing the angle of the cone), as they respectively limit the concentration and modify the distance between the reflector and the focal point. Finally, manufacturing and installation errors lead to an increase in the size of the heat flux distribution or a distortion of its shape. The angle of the cone in which an incident beam is likely to be reflected may increase according to the quality of the reflecting material and its cleanliness, because the reflected radiation may be slightly scattered (imperfect specularity). The shape of the heat flux distribution can be distorted by errors in the shape of the reflector due to its construction and bending; the orientation of the reflection may be deviated by misalignment of the mirrors; and system settings such as sun tracking, orientation of the reflector axis (azimuth and tilt) and the relative position of the reflector and receiving screen may also modify the shape of the heat flux distribution.

Among the latter parameters, the inclination of the receiving screen can be questioned. Indeed, a paraboloid theoretically reflects rays coming parallel to its axis at a point, whereas in reality the rays are concentrated in a zone around this point. So how to define a reception plane, improperly called the focal plane? For example, it can be vertical, normal to the axis of rotation of the reflector or normal to the bisector of the extreme rays. This choice is particularly important because distortions in the shape of the heat

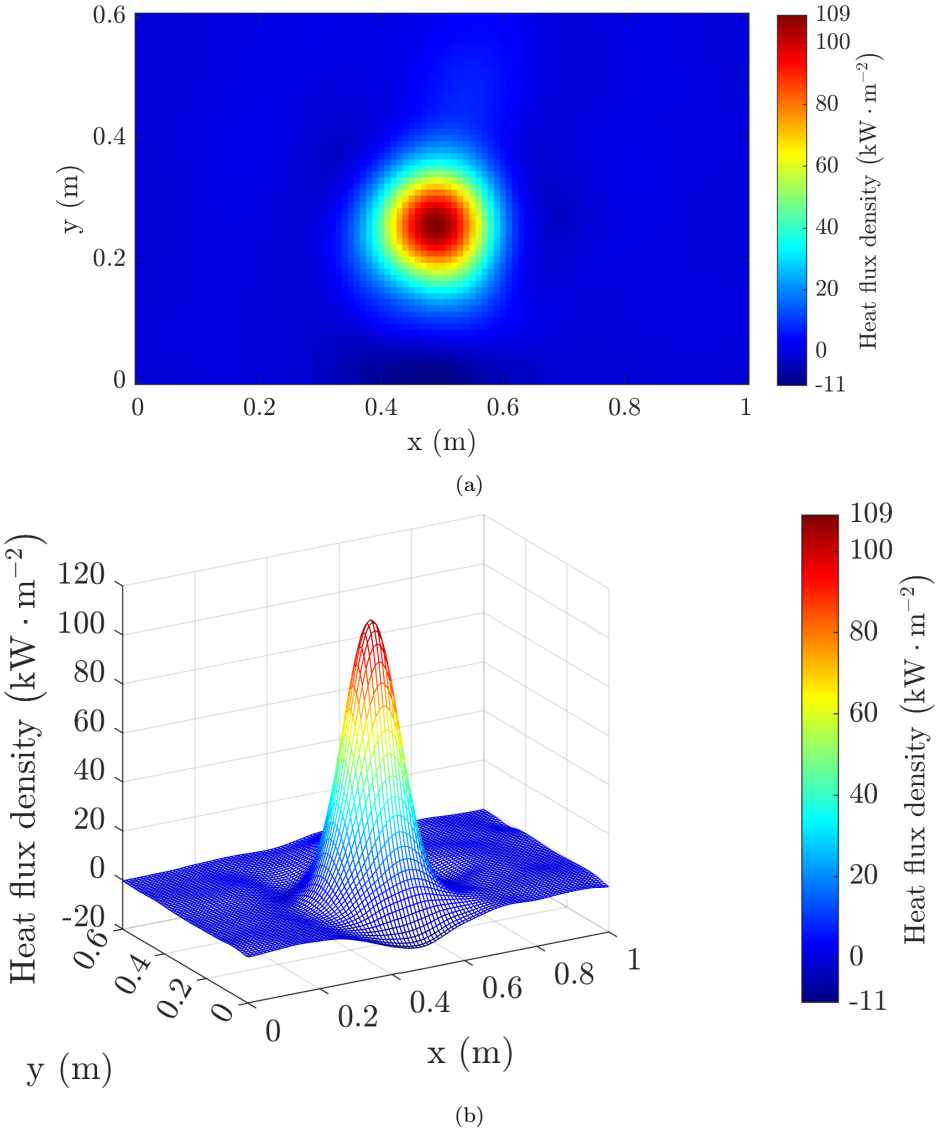

Figure D.13: Experimental heat flux map in a 2D representation (a) and in a 3D representation (b) for the first measurement on 22 March 2023.

flux distribution will be observed depending on this choice. Nevertheless, it should be kept in mind that the characteristics of the heat flux delivered by the reflector are explored in order to improve the design of the absorber or secondary optics of a system incorporating a Scheffler reflector. Therefore, the receiving screen should be roughly representative of an absorber (e.g. it

should have a fixed inclination angle). In addition, the experimental data must be comparable to the literature. In the present work, the observation plane was chosen to be vertical to facilitate the measurements.

The measurement itself could also lead to inaccuracies. A lot of work, presented in Section 2, has been done to make it reliable and the main parameter that could be discussed would be the convective exchange coefficient; although its order of magnitude is rather certain. Nevertheless, like any measurement method, there are limitations. In this case, the method leads to an almost negligible spatial smoothing of the heat flow variations, due to lateral conduction in the cast iron slab. Indeed, the phenomenon is taken in consideration in the thermal model of the cast-iron slab. Moreover, this lateral heat transfer is low due to the small thickness of the slab and its conductivity. Finally, it is not expected to observe abrupt heat flux variations given the size of the mirrors of the reflector. There is, however, a temporal smoothing due to diffusion. This implies that the results of the measurement are influenced by the "thermal history" of the cast-iron slab. To give an order of magnitude, the 95 % step response time has been roughly estimated at 40 min. But as the course of the Sun is slow and other parameters are stable, the system is studied in quasi steady state and no quick changes are expected.

References

[1] A. Munir, O. Hensel, W. Scheffler, Design principle and calculations of a Scheffler fixed focus concentrator for medium temperature applications, Solar Energy 84 (8) (2010) 1490–1502. doi:10.1016/j.solener.2010.05.011.
URL https://www.sciencedirect.com/science/article/pii/S0038092X10002021

[2] H. Naik, P. Baredar, A. Kumar, Medium temperature application of concentrated solar thermal technology: Indian perspective, Renewable and Sustainable Energy Reviews 76 (2017) 369–378. doi:10.1016/j.rser.2017.03.014.
URL https://www.sciencedirect.com/science/article/pii/S1364032117303313

[3] U. Oelher, W. Scheffler, The Use of Indigenous Materials for Solar Conversion, Solar Energy Materials and Solar Cells 33 (3) (1994) 379–387. doi:10.1016/0927-0248(94)90239-9.
URL https://www.sciencedirect.com/science/article/pii/0927024894902399

[4] D. S. Reddy, M. K. Khan, M. Z. Alam, H. Rashid, Design charts for Scheffler reflector, Solar Energy 163 (2018) 104–112. doi:10.1016/j.solener.2018.01.081.
URL https://www.sciencedirect.com/science/article/pii/S0038092X18301026

[5] E. A. Dib, F. A. S. Fiorelli, Scheffler Paraboloidal Concentrator Image Analysis, in: Proceedings of the 23rd ABCM International Congress of Mechanical Engineering, Rio de Janeiro, Brazil, 2015, p. 8. doi:10.20906/CPS/COB-2015-0893.
URL http://www.swge.inf.br/proceedings/paper/?P=COB-2015-0893

[6] D. S. Reddy, M. K. Khan, Design and ray tracing of multifaceted Scheffler reflector with novel crossbars, Solar Energy 185 (2019) 363–373. doi:10.1016/j.solener.2019.04.083.
URL https://www.sciencedirect.com/science/article/pii/S0038092X1930430X

[7] D. Fontani, P. Sansoni, F. Francini, F. Toni, D. Jafrancesco, Optical Raytracing Analysis of a Scheffler Type Concentrator, Energies 15 (1) (2022) 260, number: 1 Publisher: Multidisciplinary Digital Publishing Institute. doi:10.3390/en15010260.
URL https://www.mdpi.com/1996-1073/15/1/260

[8] I. Ayub, A. Munir, W. Amjad, A. Ghafoor, M. S. Nasir, Energy- and exergy-based thermal analyses of a solar bakery unit, Journal of Thermal Analysis and Calorimetry 133 (2) (2018) 1001–1013. doi:10.1007/s10973-018-7165-3.
URL https://doi.org/10.1007/s10973-018-7165-3

[9] T. Kanyowa, G. V. Nyakujara, E. Ndala, S. Das, Performance Analysis of Scheffler Dish Type Solar Thermal Cooking System Cooking 6000 Meals Per Day, Solar Energy 218 (2021) 563–570. doi:10.1016/j.solener.2021.03.019.
URL https://www.sciencedirect.com/science/article/pii/S0038092X2100205X

[10] M. Chandrashekara, A. Yadav, An experimental study of the effect of exfoliated graphite solar coating with a sensible heat storage and scheffler dish for desalination, Applied Thermal Engineering 123 (2017) 111–122.

[11] M. Chandrashekara, A. Yadav, Experimental study of exfoliated graphite solar thermal coating on a receiver with a scheffler dish and latent heat storage for desalination, Solar Energy 151 (2017) 129–145.

[12] S. Alberti, Analysis and Optimization of the Scheffler Solar Concentrator, Master's thesis, California Polytechnic State University, San Luis Obispo, California (Dec. 2014). doi:10.15368/theses.2014.183.
URL http://digitalcommons.calpoly.edu/theses/1335

[13] J.-C. Pulfer, C. Ingeniería, R. M. López, Small marmalade factory in Argentina working with Scheffler type industrial cooker, in: Proceedings of Solar Cookers and Food Processing International Conference, Granada, Spain, 2006, p. 4.

[14] S. Sasidharan, P. Dutta, Optical characterization of a fixed focus Scheffler reflector for pressurized solar receiver testing, Solar Energy 227 (2021) 89–100. doi:10.1016/j.solener.2021.08.078.
URL https://www.sciencedirect.com/science/article/pii/S0038092X21007428

[15] M. Röger, P. Herrmann, S. Ulmer, M. Ebert, C. Prahl, F. Göhring, Techniques to Measure Solar Flux Density Distribution on Large-Scale Receivers, Journal of Solar Energy Engineering 136 (3) (2014) 031013. doi:10.1115/1.4027261.
URL https://doi.org/10.1115/1.4027261

[16] E. A. Dib, Análise da formação de imagem focal do concentrador solar paraboloidal tipo scheffler, Ph.D. thesis, University of São Paulo, São Paulo, Brazil (2021).

[17] J. Gaspar, Y. Corre, M. Firdaouss, J. L. Gardarein, J. Gerardin, J. P. Gunn, M. Houry, G. Laffont, T. Loarer, M. Missirlian, J. Morales, P. Moreau, C. Pocheau, E. Tsitrone, First heat flux estimation in the lower divertor of WEST with embedded thermal measurements, Fusion Engineering and Design 146 (2019) 757–760. doi:10.1016/j.fusengdes.2019.01.074.
URL https://www.sciencedirect.com/science/article/pii/S0920379619300821

[18] S. Indora, T. C. Kandpal, Institutional cooking with solar energy: A review, Renewable and Sustainable Energy Reviews 84 (2018) 131–154. doi:10.1016/j.rser.2017.12.001.
URL https://www.sciencedirect.com/science/article/pii/S1364032117315320

[19] D. Holmgren, Review of thermal conductivity of cast iron, International Journal of Cast Metals Research 18 (6) (2005) 331–345, publisher: Taylor & Francis _eprint: https://doi.org/10.1179/136404605225023153.

doi:10.1179/136404605225023153.
URL https://doi.org/10.1179/136404605225023153

[20] J. A. Duffie, W. A. Beckman, Solar Engineering of Thermal Processes, 3rd Edition, Wiley, Hoboken, USA, 2006, google-Books-ID: tPayQgAACAAJ.

[21] P. S. Bhambare, S. C. Vishweshwara, Design aspects of a fixed focus type Scheffler concentrator and its receiver for its utilization in thermal processing units, Energy Nexus 7 (2022) 100103. doi:10.1016/j.nexus.2022.100103.
URL https://www.sciencedirect.com/science/article/pii/S2772427122000651

[22] C. K. Ho, A. R. Mahoney, A. Ambrosini, M. Bencomo, A. Hall, T. N. Lambert, Characterization of Pyromark 2500 Paint for High-Temperature Solar Receivers, Journal of Solar Energy Engineering 136 (1) (Jul. 2013). doi:10.1115/1.4024031.
URL https://doi.org/10.1115/1.4024031

[23] J. Coventry, P. Burge, Optical properties of Pyromark 2500 coatings of variable thicknesses on a range of materials for concentrating solar thermal applications, in: AIP Conference Proceedings, Vol. 1850, American Institute of Physics, 2017, p. 030012. doi:10.1063/1.4984355.
URL https://aip.scitation.org/doi/abs/10.1063/1.4984355

[24] S. Caron, J. Garrido, E. Setien, R. Harzallah, L. Noč, I. Jerman, M. Röger, F. Sutter, Forty Shades of Black: A Benchmark of High Temperature Sprayable Black Coatings Applied on Haynes 230, in: AIP Conference Proceedings, Vol. 2303, AIP Publishing, Daegu, South Korea, 2020, p. 150007. doi:10.1063/5.0028773.
URL https://aip.scitation.org/doi/abs/10.1063/5.0028773

[25] Y. S. Touloukian, R. W. Powell, C. Y. Ho, P. G. Klemens, Thermophysical properties of matter - the TPRC data series. Volume 2. Thermal conductivity - nonmetallic solids. (Reannouncement). Data book, Tech. Rep. AD-A-951936/4/XAB, Purdue Univ., Lafayette, IN (United States). Thermophysical and Electronic Properties Information Center (Jan. 1971).
URL https://www.osti.gov/biblio/5303523